Modeling and Optimal Design of an Eddy Current Coupling for Slip-Synchronous Permanent Magnet Wind Generators

Zac Mouton, *Student Member, IEEE*, and Maarten J. Kamper, *Senior Member, IEEE*

***Abstract*—In this paper, the possibility of using an eddy current slip coupling to remove cogging torque and torque ripple in a slip-synchronous permanent magnet wind generator is investigated. Two different topologies are proposed. It is shown that two-dimensional (2-D) finite-element methods are inaccurate compared to three-dimensional (3-D) finite-element methods when solving eddy currents in eddy current couplings. The 3-D finite-element transient simulations are validated using a manufactured prototype 15-kW eddy current coupling. An analytical approximation is developed and used for the design optimization of two eddy current coupling topologies. Using the optimally designed eddy current coupling, it is shown that the analytical and 3-D finite-element solutions compare very well and that the proposed eddy current coupling topology has no torque ripple. The analytical approximation is well suited to the rapid design optimization of eddy current couplings that use a conductive material in the air gap.**

***Index Terms*—Cogging torque, design, eddy currents, finite element, optimization, permanent magnet (PM), wind generator.**

NOMENCLATURE

Δ_i	Arc length between the center and the side of the current loop (in meters).
b	Magnitude ratio between the flux density and its fundamental harmonic.
$B_{\rm ag}$	Analytically calculated air gap flux density (in tesla).
$B_{\rm FE}$	Air gap flux density determined by finite-element simulation (in tesla).
B_g	Air gap flux density (in tesla).
B_{g1}	Peak of the fundamental air gap flux density (in tesla).
B_r	Residual magnetic flux density (in tesla).
B_s	Inner yoke flux density (in tesla).
B_y	Outer yoke flux density (in tesla).
C	Vertical axis offset.
dx	Small element arc length (in meters).
dy	Small element length (in meters).
$d\theta$	Small element angle (in radians).
$e_{\rm elm}$	Instantaneous induced element voltage (in volts).
e_i	Induced loop voltage (in volts).
F_i	Instantaneous force generated by loop current (in newtons).
$F_{\rm pp}$	Instantaneous force generated per pole (in newtons).
H_c	Coercive magnetic field strength (in amperes per meter).
h_c	Radial height of the conductive material (in meters).
H_g	Air gap magnetic field strength (in amperes per meter).
H_m	Permanent magnet (PM) magnetic field strength (in amperes per meter).
h_m	Radial height of the PM (in meters).
H_s	Inner yoke magnetic field strength (in amperes per meter).
h_s	Radial height of the inner yoke (in meters).
H_y	Outer yoke magnetic field strength (in amperes per meter).
h_y	Radial height of the outer yoke (in meters).
i	Number of specific current loop.
i_i	Induced current in the specific current loop (in amperes).
K_y	Eddy current coupling constant (in meters).
l_c	Axial length of the conductive material (in meters).
l_g	Radial length of the air gap(s) and conductive material (in meters).
l_{ipg}	Arc length between two adjacent magnets (in meters).
$l_{\rm pm}$	Axial length of the PM (in meters).
l_s	Axial length of the inner yoke (in meters).
l_y	Axial length of the outer yoke (in meters).
m	Gradient of a straight line.
n	Number of current loops per pole.
p	Number of poles.
r_c	Effective radius of the conductive material (in meters).
R_i	Electrical resistance of current loop i (in ohms).
$r_{\rm pm}$	Effective radius of the PM (in meters).
r_s	Effective radius of the inner yoke (in meters).
r_y	Effective radius of the outer yoke (in meters).
T_A	Torque determined by analytical calculation (in newton meter).
$T_{\rm FE}$	Torque determined by finite-element simulation (in newton meter).
y_{ai}	Axial length of current loop i in the magnetic field (in meters).
y_i	Axial length of current loop i (in meters).
μ_m	Permeability of the PM material (in henry per meter).
ρ_c	Resistivity of the conductive material (in ohms per meter).
τ_p	Arc length of a pole pitch (in meters).
$\tau_{\rm pm}$	PM arc length to pole pitch ratio.
ω_{re}	Electrical frequency of slip rotor (in radians per second).

Manuscript received January 31, 2013; revised June 22, 2013; accepted August 4, 2013. Date of publication September 18, 2013; date of current version January 31, 2014. This work was supported in part by the National Research Foundation of South Africa.

The authors are with the Department of Electrical and Electronic Engineering, Stellenbosch University, Matieland 7602, South Africa (e-mail: kamper@sun.ac.za).

Digital Object Identifier 10.1109/TIE.2013.2282602

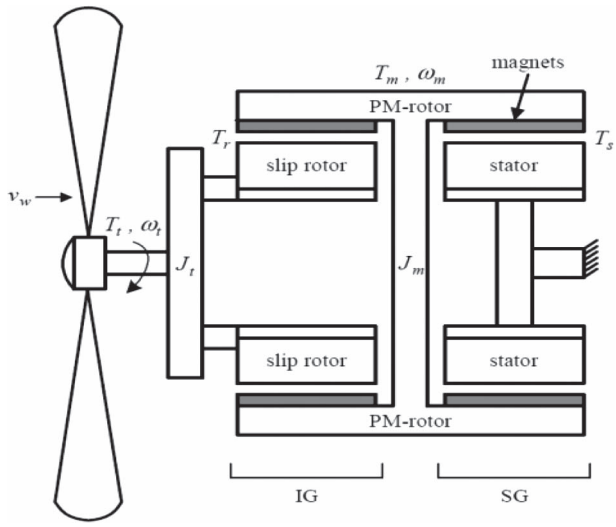

Fig. 1. Concept diagram of the SS-PMG.

I. Introduction

In THIS study, the focus is on the optimal design of an eddy current coupling as part of a small-scale 15-kW slip-synchronous PM wind generator (SS-PMG). The SS-PMG, first introduced in [1], effectively combines the functionality of an induction generator (IG) and a synchronous generator (SG). The result is a direct-drive (gearless) direct-grid-connected generator system.

In [2], it is stated that torque quality and cost are the two most important aspects in the design of a direct-drive PM wind generator. Torque ripple generates unwanted noise and vibrations, and related high cogging torque can prevent start-up due to low torque generation at low turbine speeds. The torque ripple is mainly generated by the slotted stator and by the placing of windings and PMs [3]. In [1], it was found that the IG component of the SS-PMG is very susceptible to construction and material inequalities, which create cogging torque and add to the torque ripple. The SS-PMG investigated in [1] has a full load torque ripple of 2% according to finite-element analysis and a measured cogging torque of 4.5%. In [4], five machine configurations, all using cage type of windings and called slip PM generators, are designed for use as the IG component of the SS-PMG. In this paper, an additional alternative for use as the IG component of the SS-PMG, namely, the eddy current coupling proposed in [5], is investigated. The aim is the complete removal of cogging torque and torque ripple in the transfer of torque from the turbine to the SG component of the SS-PMG.

II. SS-PMG Concept

The SS-PMG has undergone considerable development in recent years. It was introduced and described in [1] as an expansion of the PM induction generator concept discussed in [6].

The SS-PMG consists of a stator, a PM rotor, and a slip rotor, as shown in Fig. 1. The stator is connected to the grid, with the free-rotating PM rotor operating at synchronous speed in relation to the stator's rotating field. The combination of these two components creates the SG component of the SS-PMG. The short-circuited slip rotor rotates at slip speed relative to the PM rotor, creating the IG component of the SS-PMG. The slip rotor is mechanically connected directly to the wind turbine. Power transfer takes place from the turbine to the slip rotor and then via the PM rotor to the stator and the grid.

The SS-PMG is an attractive generator topology, particularly because no gearbox and no power electronic converter are necessary. Another attractive feature of the SS-PMG is that it can be used in a wind farm, potentially allowing maximum power point tracking [1], [7]. Wind farm technology has undergone a lot of development [8]–[12]. The SS-PMG does need a synchronization method with the grid, which is developed in [13]. In [13], it is shown that the SS-PMG can make a direct grid connection in a stable automated manner throughout the usable wind range, using the synchronization controller developed for the SS-PMG.

A transient model is developed for the SS-PMG in [14]. It is shown that the SS-PMG handles transient turbine torque well. Torque quality, however, is very important in the SS-PMG, particularly on the low-frequency IG side. Ripples carried through the free-rotating PM rotor will influence the quality of the electrical power generated, especially low-frequency and high-amplitude ripples. In order to ensure sustained internal stability, it is preferred that there be no cogging torque and no load torque ripple.

The SS-PMG requires minimal maintenance, is affordable due to no gearing or converter being necessary, offers grid voltage support [13], and is stable under external transient torque conditions. It is ideally suited for high average wind speed sites.

III. Eddy Current Coupling Concept

Eddy current couplings are old concepts [15], [16]. For decades, this concept has been successfully implemented in industry for various purposes. It is used in variable speed drives, in electronic clutches, in fluid control in power drives, and in mechanically isolating a motor from its load.

In the SS-PMG wind generator application, the eddy current coupling transfers torque from the wind turbine to the SG while mechanically isolating the one from the other. The main advantage of this setup is that the eddy current coupling will damp the majority of the vibrations and disturbances of the turbine [14]. A spring and damper analogy of the turbine and SS-PMG is explained in [13].

Eddy current couplings typically consist of a loss drum and a field member. The field member provides the magnetic field, in this case using PMs. As the loss drum rotates relative to the magnetic field, eddy currents are induced in the loss drum. The magnitude of the induced eddy currents depends on machine constants and the frequency of the magnetic field relative to the drum, as explained in [15]. The transfer of power is dependent on the difference in speed of the two components, known as the slip speed.

When applying the eddy current coupling concept to the SS-PMG, the IG side of the PM rotor serves as field member, and the slip rotor serves as loss drum.

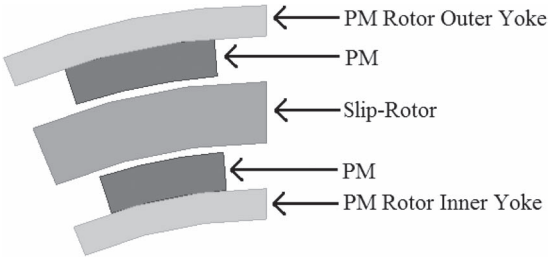

Fig. 2. Topology 1): double-sided PM topology using magnets on both sides of the slip rotor and two air gaps (DSR).

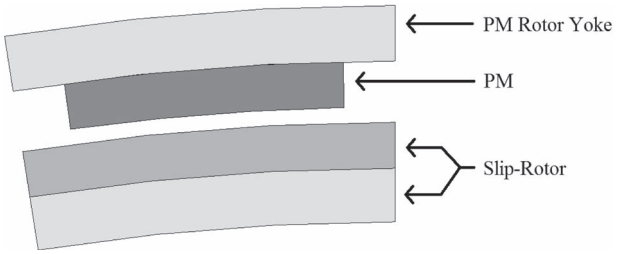

Fig. 3. Topology 2): single-sided PM topology using magnets on only one side of the slip rotor and one air gap (SSR), with the slip rotor consisting of mixed material.

IV. Eddy Current Coupling Topologies

For operation in the SS-PMG, the eddy current coupling is to be designed to operate at a certain rated torque and at high efficiency. Because it is to be used in a wind turbine generator (WTG), the coupling's mass has to be kept to a minimum in the design. In order to remove cogging torque and torque ripple completely, as well as to reach the high torque and efficiency requirements of the eddy current coupling, a featureless loss drum with high conductivity has to be used. Using a conductive material with a smooth surface and no slots ensures no torque ripple as shown by [5].

Various topologies of the eddy current coupling are possible for application in the SS-PMG. The two topologies evaluated in this study are the following:

1) double-sided PM rotor (DSR) topology using magnets on both sides of the slip rotor and two air gaps, as shown in Fig. 2;
2) single-sided PM rotor (SSR) topology using magnets on only one side of the slip rotor and one air gap, as shown in Fig. 3.

Note that, for the DSR topology, the outer and inner PM rotor yokes both form part of the PM rotor component. This topology has the important advantage of no magnetic attraction forces between the slip rotor and the PM rotor. The SSR topology uses a mixed material slip rotor, consisting of the conductive material and the inner yoke. In Fig. 4, the dimensions to be optimally designed are shown using the SSR topology as an example. In addition to the dimensions shown in Fig. 4, the axial lengths of the conductive material (l_c) and the magnets $(l_{\rm pm})$ also have to be optimally designed.

In [5], it is shown that, using the same PM material and operating at the same slip speed, the SSR topology produces 34.4% more torque than an alternative eddy current coupling topology. The alternate topology differs from the DSR topology in that it uses PMs on only one side of the slip rotor.

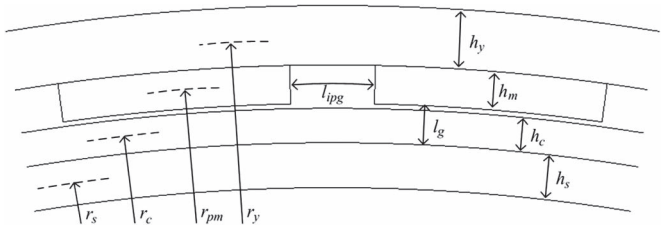

Fig. 4. Dimension symbols shown using the SSR topology.

Fig. 5. Prototype loss drum (left) and DSR PM rotor (right).

TABLE I
Dimensions of Small Prototype of Fig. 5

Dimension	air gap	h_c	h_y	p	τ_{pm}	r_c	l_{pm}	l_c
Value	1 mm	8	4	16	0.593	76	35	82

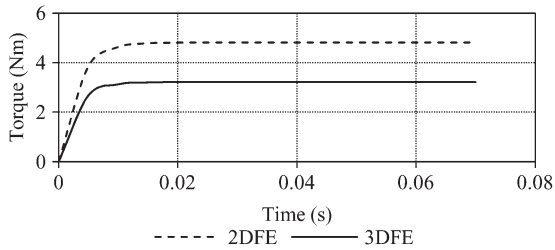

Fig. 6. Solving torque in 2-D and 3-D FE transient simulations of the DSR topology of Fig. 5 at 4% slip.

V. Eddy Current Coupling FE Analysis

In [5], the small prototype eddy current coupling, shown in Fig. 5 and with the dimensions listed in Table I, is tested and compared to two-dimensional (2-D) and three-dimensional (3-D) FE simulation results. All FE simulations are transient FE simulations done using JMAG Designer software. The 2-D and 3-D FE transient simulations of the prototype are done at a 4% slip speed, which correlates to an efficiency of 96%. The resulting torque is smooth and without any indication of torque ripple, as shown in Fig. 6 for both FE solutions.

In Fig. 7, the torque versus slip behavior of the 2-D and 3-D FE simulated models are shown, as well as the measured torque versus slip behavior of the small prototype. There is a significant difference between the 2-D FE simulated and measured values, whereas the results of the 3-D FE simulations match the measured values almost exactly.

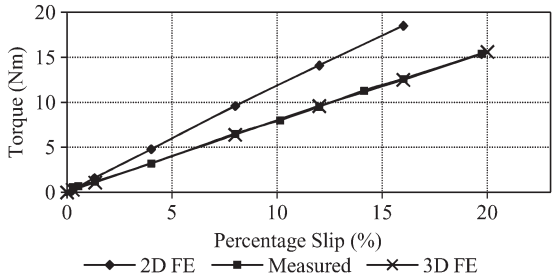

Fig. 7. Transient FE and measured results of torque versus slip of the DSR topology of Fig. 5.

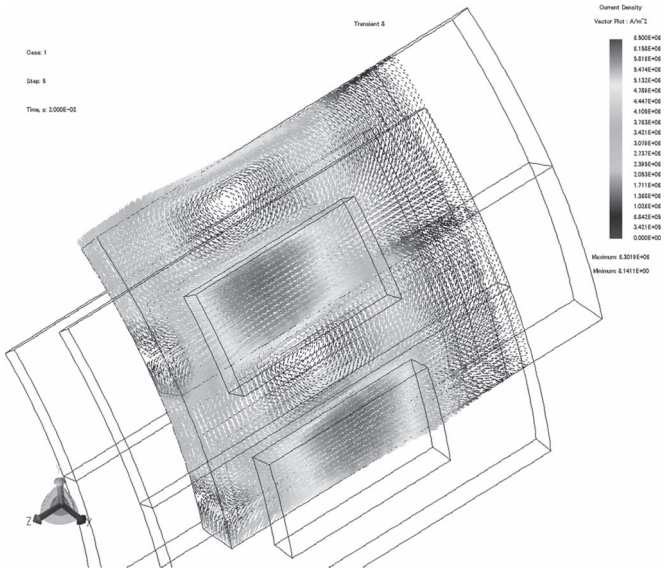

Fig. 8. Current density plot of the prototype as generated by 3-D FE transient simulation in JMAG.

In Fig. 8, a current density vector plot of two poles of the machine in Fig. 5 is shown as calculated in the 3-D FE simulation. It is clear that the induced currents follow a circular pattern and do not flow in only an axial direction underneath the magnets, as is assumed in most literature where similar machines are analyzed [15], [17]. Thus, the eddy current density varies in the axial direction and does not remain constant as in 2-D FE simulations. The axial length of the slip rotor (l_c), i.e., longer than the magnet's active length $(l_{\rm pm})$, also has a significant effect on the torque since it influences the available path for the return current. Because 2-D FE simulations do not include these effects, they yield inaccurate results. Consequently, 3-D FE simulations are used for the study of the proposed eddy current coupling topologies.

In [17], an axial flux eddy current brake is simulated using a 3-D FE package. The difficulties of 3-D FE simulation are stated, the most significant of which is the accurate solving of the transient eddy currents in ferromagnetic materials. In this paper, almost all of the eddy currents are induced in a nonferromagnetic material. The scarcity of publications that compare 3-D FE results with measured results where eddy current is a predominant factor is an indication of the difficulty involved with accurate 3-D simulation [17]. It was found that the JMAG FE software performed very well for the particular concept used in this study.

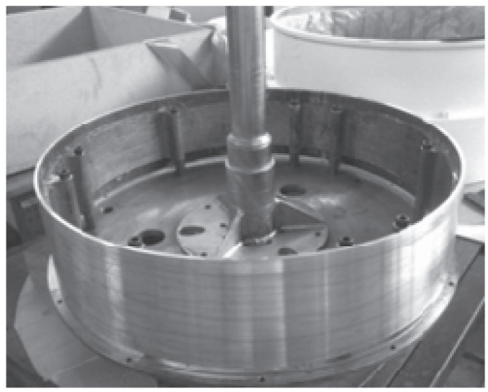

Fig. 9. Slip rotor assembled on front-plate with shaft connected.

TABLE II
DIMENSIONS OF THE MANUFACTURED SLIP ROTOR

Dimension	Value
air gap	0.75 mm
h_c	5.35 mm
h_s	7 mm
p	40
τ_{pm}	0.73
r_c	316.85 mm
l_c	148 mm

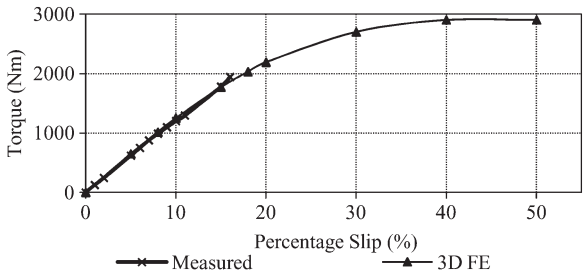

Fig. 10. Torque versus slip characteristics of the prototype eddy current coupling [5].

VI. Slip Rotor Prototype

In [5], a slip rotor is designed to operate with an existing PM rotor as an eddy current coupling for a 15-kW SS-PMG wind generator. It reaches the designed operating torque of 1000 N · m at a slip of 8%, corresponding to 92% efficiency. The designed SSR eddy current coupling is manufactured and tested. The constructed slip rotor is shown in Fig. 9, and its dimensions are given in Table II. The measured torque versus slip behavior is compared with 3-D FE simulated results in Fig. 10. The torque measurement was limited to values below 2000 N · m by the equipment used. The FE prediction compares very well with the measured values, with less than 4.5% error throughout the measured range. Thus, to conclude, 3-D FE transient simulations may be used as an acceptable representation of reality for the proposed eddy current coupling topologies.

VII. Analytical Approximation

In literature, analytical models for eddy current couplings are usually based on Maxwell's laws. However, accurately

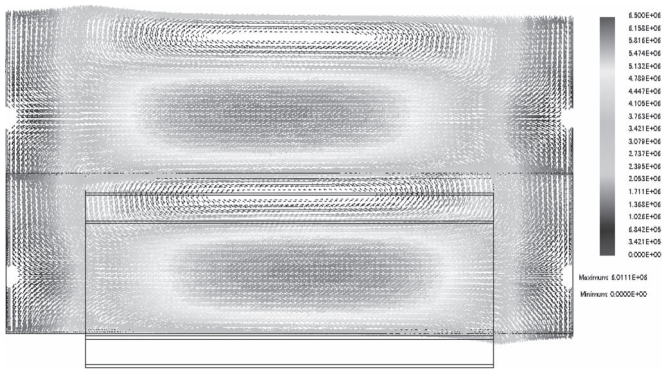

Fig. 11. JMAG current density plot of the 3-D FE eddy current coupling model simulated at a 3% slip. The position of the magnet is also shown.

determining such a model is extremely complex due to the current distribution being unknown, the varying permeabilities of the materials in the eddy current coupling, and the 3-D behavior that has to be modeled [15], [16]. There are a few examples in literature of 3-D analytical models for eddy current couplings; however, dubious assumptions are made regarding the behavior of the eddy currents [15], [16]. For the coupling proposed in this study, the model is further complicated by the addition of the conductive ring.

An analytical model based on common electrical laws, such as those of Faraday and Ohm, is proposed in this study. The challenge with this approach is that there are no specifically defined current paths, due to the featureless conductive material of the slip rotor. However, through observations made using modern 3-D FE simulation technology, a model for the current path is developed for low slip frequencies.

Given the dimensions h_m, h_c (thus, also l_g), and $l_{\rm pm}$ in Fig. 4, the analytical model determines the dimensions h_y, h_s, and l_c and calculates the torque of the eddy current coupling. In [5], it is found that the conductor end lengths may be designed as 50% of a pole pitch, leading to

$$l_c = \tau_p + l_{\rm pm} \tag{1}$$

where τ_p is the arc length of a single pole pitch.

A. Current Path Model

When studying the current density plot of the conductive component of the slip rotor, as simulated in JMAG and shown in Fig. 11, it is evident that the eddy currents tend to follow circulating paths symmetrically across an axis between the magnet poles. These current paths may be modeled as n consecutive concentric current loops covering an entire pole pitch in the slip rotor as shown in Fig. 12. The center of these concentric loops is in the middle between two magnetic poles. The y-axis in Fig. 12 is in the axial direction, and the x-axis is in the tangential or arc direction.

Every current loop i has $2i$ smaller elements in the arc length, each of tangential width $dx = r_c d\theta$, axial length dy, and depth h_c. A single element is shown in its loop in Fig. 13. As shown in Fig. 13, the tangential or arc length width of current loop i is $2\Delta_i$, and y_i is the axial length of the loop. K_y in Fig. 12

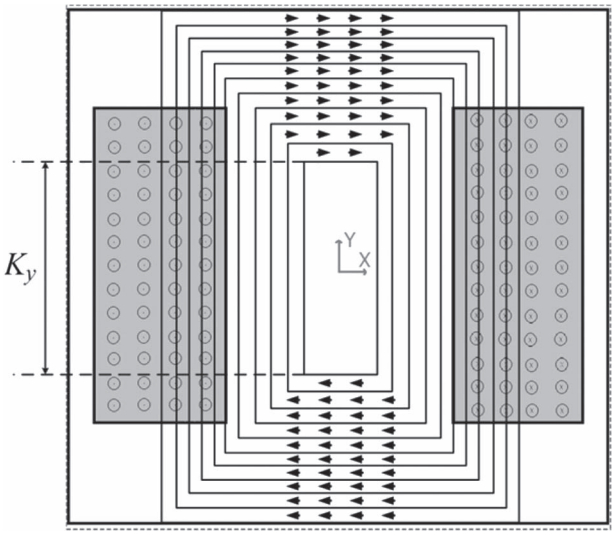

Fig. 12. Model of concentric current loops.

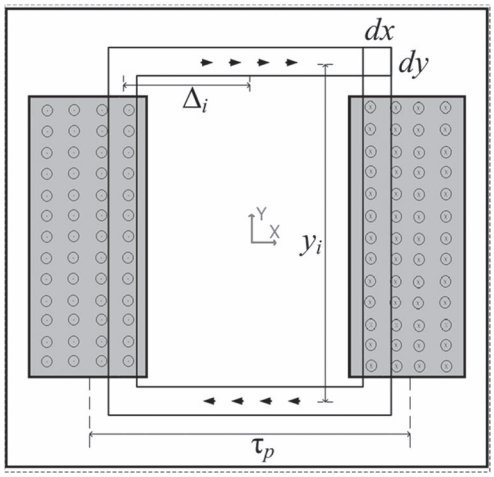

Fig. 13. Model of individual current loop.

is an axial length that defines the region where the axial eddy current flow starts to turn to flow in the tangential direction. K_y is a constant for a particular eddy current coupling. It has a significant effect on the accuracy of the analytical model and is discussed separately in Section VIII.

From the previous discussion and from Figs. 12 and 13, if dx is a small chosen arc width, the following are calculated:

$$n = \frac{\tau_p}{2dx} \tag{2}$$

$$\Delta_i = idx \text{ with } i = 1, 2, \ldots, n \tag{3}$$

$$dy = \frac{l_c - K_y}{2n} \tag{4}$$

$$y_i = K_y + 2idy. \tag{5}$$

Finally, the axial active length of current loop i (y_{ai}) is calculated as

$$y_{ai} = \begin{cases} y_i & y_i \le l_{\rm pm} \\ l_{\rm pm} & y_i > l_{\rm pm}. \end{cases} \tag{6}$$

B. Flux Density Calculation

The calculation of the air gap flux density follows a similar approach as in [18]. The MMF equation of a single pole pitch of an eddy current coupling of the SSR topology is

$$H_c h_m = H_y l_y + H_m h_m + H_g l_g + H_s l_s \tag{7}$$

with l_y and l_s being the approximated arc lengths of pole pitches in the outer and inner yokes, respectively. l_g is the effective radial length of the air gap, i.e., the combination of the conductor radial thickness and the actual air gap radial length as shown in Fig. 4. H_y and H_s are the field strengths in the yokes, H_m is the field strength in the magnets, H_g is the field strength in the air gap, and H_c is the coercive magnetic field strength. h_m is the PM thickness, as shown in Fig. 4.

Considering that $\mu_m = B_r/H_c$ for the linear region of the PM material and making the assumption that the flux densities in the air gap and the magnets are the same, the flux density in the air gap is

$$B_{\mathrm{ag}} = \frac{H_c h_m - H_y l_y - H_s l_s}{\left(\frac{H_c}{B_r}\right) h_m + \frac{l_g}{\mu_0}}. \tag{8}$$

In (8), H_c and B_r are constants of the magnetic material that are dependent on temperature. Based on the measurement taken during the tests done on the prototype in [5], it is estimated that the eddy current coupling will operate at a temperature of approximately 60 °C.

C. Calculation of Yoke Thickness

The yoke thicknesses may be determined by choosing a fixed flux density in the steel, which ensures that the field strength in the steel in (7) is constant. Thus, the yoke thickness may be determined in a similar manner to what is done in [18] by

$$h_y = \frac{l_y \tau_{\mathrm{pm}}}{2}\left(\frac{B_{\mathrm{ag}}}{B_y}\right) \quad h_s = \frac{l_s \tau_{\mathrm{pm}}}{2}\left(\frac{B_{\mathrm{ag}}}{B_s}\right) \tag{9}$$

where τ_{pm} is the ratio of the magnet pitch to the pole pitch and B_y and B_s are the chosen flux densities in the steel. The flux densities in the yokes are chosen to be $B_y = B_s = 1.4$ T when using M470-50A steel; hence, the corresponding magnetic fields are $H_y = H_s = 500$ A/m.

It is necessary to make an initial assumption of the yoke thicknesses to calculate l_y and l_s and, hence, an initial value for the air gap flux density according to (8). Choosing the initial yoke thicknesses equal to the magnet height is found to be a good first approximation. Using the newly calculated air gap flux density in (9), more accurate yoke thicknesses are calculated. This process is repeated until there is no more change in either flux density or yoke thickness.

D. Stray Flux Constraints

For (7) to be valid, stray flux between adjacent magnets has to be prevented. Thus, the same constraint principles used in [18] are applicable. For an eddy current coupling of the SSR topology, the constraints become

$$h_m > l_g \tag{10}$$

to prevent stray flux between the magnet and its yoke, and

$$l_{ipg} = \frac{2\pi r_{\mathrm{pm}}}{p}(1 - \tau_{\mathrm{pm}}) > 2 l_g \tag{11}$$

to prevent stray flux between adjacent magnets. In (11), p is the number of poles, and l_{ipg} is the tangential distance between two adjacent magnets as shown in Fig. 4. For the DSR topology, (11) becomes $l_{ipg} > l_g$, but (10) remains the same.

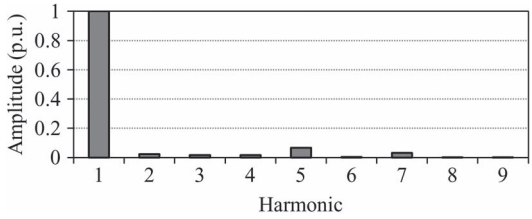

Fig. 14. Harmonic analysis of air gap flux density.

E. Flux Density Harmonics

It should be noted that (8) calculates the amplitude value of the air gap flux density in the middle of the magnet pole. In the analytical model, however, only the fundamental harmonic component of the air gap flux density is used. It is shown in Fig. 14 that the fundamental flux density harmonic is the dominant harmonic, with the other harmonics small enough to be negligible. In [18], it is shown that the air gap flux density can be closely approximated by a flat-topped trapezoidal wave. When using that approximation, the ratio b between the actual air gap flux density B_{ag} of (8) and the amplitude of its fundamental harmonic B_{g1} is

$$b = \frac{B_{\mathrm{ag}}}{B_{g1}} \approx 0.937. \tag{12}$$

This ratio depends on the magnet-to-pole-pitch ratio τ_{pm}. It was found in [19] that an optimal value for τ_{pm} is 0.7 for air-cored machines, and this value is used in this study for the eddy current couplings. Thus, the same value for b, as given by (12), is used in the analytical approximation.

F. Loop-Induced Voltage

Considering a single axial element of a current loop in a magnetic field as shown in Fig. 15 and the magnetic field described by

$$B_g = B_{g1} \sin\left(\frac{px}{2r_c}\right) \tag{13}$$

the instantaneous induced voltage of the element may be calculated similarly to [20] as

$$e_{\mathrm{elm}} = \frac{4}{p} B_{g1} \omega_{re} r_c dy \sin\left(\frac{p\Delta_i}{2r_c}\right). \tag{14}$$

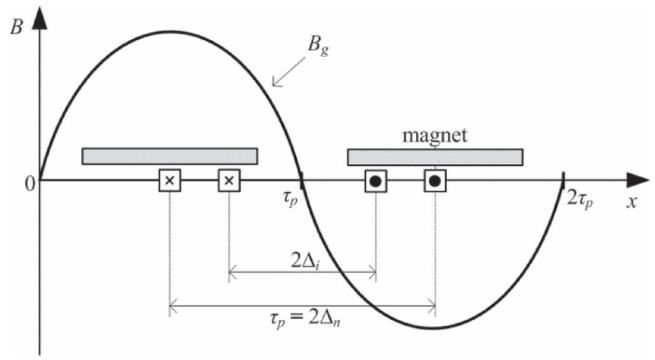

Fig. 15. Axial element of a current loop in a sinusoidal flux density wave.

Hence, in a current loop i, the induced voltage in the loop e_i is calculated from (14) as

$$e_i = 2y_{ai}\frac{4}{p}B_{g1}\omega_{re}r_c \sin\left(\frac{p\Delta_i}{2r_c}\right). \tag{15}$$

G. Loop Resistance

In general, the electrical resistance of a length of a current carrying material can be calculated as the product of the length and the material's resistivity, divided by the cross-sectional area perpendicular to the direction of current flow. When applied to current loop i in Figs. 12 and 13, the electrical resistance of the loop can be calculated by

$$R_i = 4\frac{\rho_c\Delta_i}{h_c dy} + 2\frac{\rho_c y_i}{h_c dx} \tag{16}$$

where ρ_c is the resistivity of the conductive material. From (15) and (16), it can be seen that the instantaneous induced current in the loop is $i_i = e_i/R_i$, neglecting the inductance component of the current loop in air at low slip frequencies.

H. Calculation of the Torque

When the loop current i_i is known, the instantaneous force generated by the current loop is calculated by

$$F_i = B_{g1}\sin\left(\frac{p\Delta_i}{2r_c}\right)2y_{ai}i_i. \tag{17}$$

Every concentric loop contributes to the force generated per pole. Therefore, the force generated per pole is

$$F_{\rm pp} = \sum_{i=1}^{n} F_i. \tag{18}$$

From this, the total torque generated by the eddy current coupling is calculated by

$$T_A = F_{\rm pp}pr_c. \tag{19}$$

I. Effect of Harmonics on the Calculated Torque

The proposed analytical segmented loop model suggests that higher order harmonic eddy currents, other than the fundamental, will also be induced in loops and will therefore generate harmonic torques. From (15), with both the frequency and pole number higher of the higher order air gap flux densities, the induced higher order harmonic voltages are only proportional to the amplitudes of the higher order harmonic air gap flux densities. These harmonic amplitudes, however, are shown in Fig. 14 to be very small. Also, at the much higher harmonic frequencies, the harmonic inductive impedances of the loops are relatively high. Thus, the influence of higher order harmonic eddy currents will be small. The results of transient FE analysis in Section IX also show that there is no torque ripple at low and high slip speeds.

VIII. Determining the Approximation of K_Y

Included in (4) is a constant K_y defined as the axial length for which the eddy currents in all the current loops flow in only the axial direction. K_y has a significant influence on the modeling of the current path; thus, it is important to determine K_y to be within a reasonable degree of accuracy before accepting the analytical model's results as accurate. However, determining the exact length of K_y for an eddy current coupling is difficult. The challenge of predicting K_y is that everything that has an influence on the current path should be included in the approximation of K_y.

Fortunately, studies of the preliminary optimization lead to an observation that significantly simplifies the approximation of K_y. It is observed that, for a specific pole number, the thickness-related dimensions (h_c, h_m) may be optimized, independent of the accuracy of K_y. Thus, K_y may be approximated as a function of axial length alone, for a specific number of poles.

In this approximation, the length of K_y and the pole pitch arc length are considered as ratios of the axial length of the PMs as

$$\alpha_k = \frac{K_y}{l_{\rm pm}} \tag{20}$$

$$\alpha_\tau = \frac{\tau_p}{l_{\rm pm}} \tag{21}$$

where α_k is a function of α_τ. It is found that the best approximation for α_k as a function of α_τ is a straight-line relationship of the form

$$\alpha_k \approx m\alpha_\tau + C \tag{22}$$

where m is the gradient of the line and C is the vertical axis offset, as determined using the process described in Table III. By substituting (20) and (21) in (22), it can be seen that K_y varies only with a change in the axial length of the machine, subject to the pole number being kept constant.

An accurate K_y value is determined by adjusting K_y until the analytical model's torque and 3-D FE predicted torque are the same. Thus, the torque calculated from the fundamental harmonic flux density is approximated as equal to the actual torque.

In Fig. 16, the gradient line approximation for α_k and some actual values are shown for a 40-pole machine of the SSR topology. The approximation of (22) is a good match to the actual values of α_k, with the greatest error being 2.2% for α_k

TABLE III
STEPS TO DETERMINE THE GRADIENT PARAMETERS OF (22)

Step	Action
1	Do a preliminary design optimisation iteration of the eddy current coupling, for the specific pole count, using a K_y value of $0.75l_{pm}$. Ignore the result of l_{pm}.
2	Using the values of h_c and h_m determined in step 1, do two 3D FE simulations for two different magnet lengths to determine T_{FE} for two α_τ values. The two α_τ values are determined by using (21). Use l_c as determined by (1).
3	For the two α_τ values of step 2, determine accurate K_y values where $T_A = T_{FE}$, by comparing the analytical torque results with the results of the two 3D FE transient simulations of step 2.
4	Use the accurate values of K_y in (20) to calculate the two α_k values for the corresponding α_τ values.
5	The determined α_k and α_τ values give two coordinates on the line approximation of (22), as seen in the example of Fig. 16. Use the coordinates to determine m and C of (22).

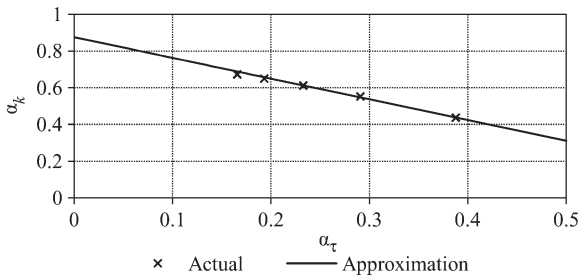

Fig. 16. Comparison of the straight-line approximation and actual values of α_k as a function of α_τ of a 40-pole machine.

TABLE IV
DESIGN CONSTRAINTS OF THE EDDY CURRENT COUPLING

Parameter	Value
Rated torque (Nm)	1000
Rated slip (%)	3
Breakdown torque (pu)	≥ 2.0
Synchronous speed (rpm)	150
Outside diameter (mm)	653.5

of the eddy current coupling with a PM length of 280 mm. This small error leads to an acceptable 1.6% error in the torque calculation.

IX. DESIGN OPTIMIZATION

The design optimization is done using the VisualDoc [21] optimization suite. The analytical model is implemented as a MATLAB function and is used by VisualDoc.

The SSR and DSR topologies are optimized for minimum active mass, subject to the torque (1000 N · m) and efficiency (97%) constraints in Table IV. It must be noted that, while the objective of minimum active mass is chosen, it is not necessarily the best for global design optimization of WTGs. The breakdown torque is a design requirement, but from the tests on the prototype of Section VI, it is a requirement easily met by the proposed topologies. Therefore, it is not included in the optimizing algorithm but is tested using FE solutions after the optimization has been done. Optimization is done

TABLE V
OPTIMIZATION RESULTS OF THE SSR TOPOLOGY

p	30	40	60	80
l_{pm} (mm)	119.7	139.6	211	337
h_y (mm)	14.58	11.36	7.85	5.96
h_c (mm)	7.51	5.25	2.9	1.7
h_m (mm)	18.8	15.7	11.7	9.1
B_{FE} (T)	0.845	0.86	0.87	0.86
T_{FE} (Nm)	1007	995	1005	1025
Mass (kg)	94.5	84.94	87.3	104
Torque Error (%)	0.79	1.2	0.3	1.5

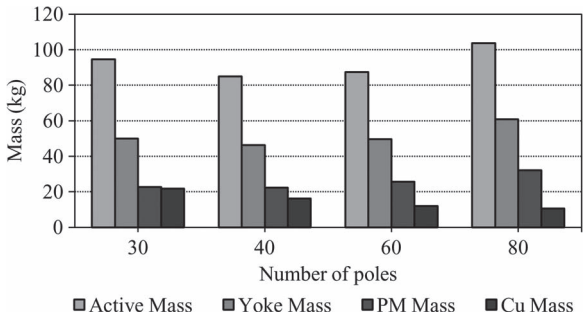

Fig. 17. Comparison of component and active mass for optimized SSR eddy current couplings.

for different pole numbers of both topologies. Copper is used as the conductive material. The strongest available magnet grade should be used in the design of air-cored radial flux PM machines [18]. Grade N48H NdFeB PM material is used in this design.

A. Optimization Results

In Table V, the results of the optimization for the different pole counts of the SSR topology are compared. The given dimensions are as determined by the optimization algorithm and analytical model, and the given air gap flux density and torque are as determined by the 3-D FE simulations done to confirm the optimization results. The percentage error given in Table V is the error of the analytical model's torque compared to the 3-D FE simulation's torque. The masses of the different components are compared for the different numbers of poles in Fig. 17.

The same process is repeated for the DSR topology, of which the results are given in Table VI, and the masses of the components are compared in Fig. 18.

B. Comparison of the Topologies' Optimization Results

The optimum design for minimum mass for the SSR topology is shown to be a 40-pole machine, and for the DSR topology, it is a 60-pole machine. The stray flux constraints of (10) and (11) limit the conductive material's thickness. Thus, h_c is very thin, and $l_{\rm pm}$ is very long for higher pole numbers, which results in increased mass. The optimal design for minimum mass is a balance between pole number and $l_{\rm pm}$.

Of the two topologies, the DSR tends to be of significantly lower mass. Due to the PMs on both sides of the copper, the

TABLE VI
OPTIMIZATION RESULTS OF THE DSR TOPOLOGY

p	30	40	60	80
l_{pm} (mm)	80.9	87.5	123.8	190.4
h_y (mm)	14.6	11.3	7.6	5.69
h_c (mm)	12.46	9.23	5.26	3.13
h_m (mm)	16.42	14.3	10.03	7.63
B_{FE} (T)	0.82	0.83	0.83	0.82
T_{FE} (Nm)	1021	985	985	990
Mass (kg)	83.75	71	65.32	72.6
Torque Error (%)	1.4	2.2	2.3	1.7

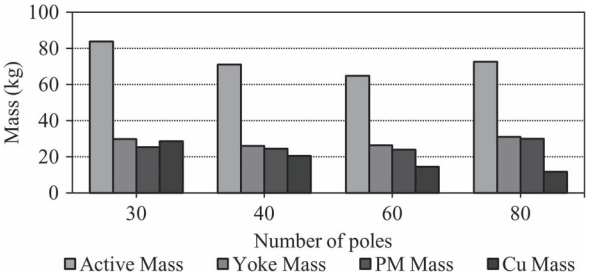

Fig. 18. Comparison of component and active mass for optimized DSR eddy current couplings.

constraints limiting h_c allow for a greater h_c for the same number of poles, leading to a shorter machine length and lower active mass in this topology.

The PM mass used in the eddy current couplings is very high, although that is expected for air-cored machines such as the eddy current coupling. It is interesting to note that the two topologies use approximately the same mass of PM material, but the SSR uses significantly more yoke mass. This is due to a significantly larger h_m, which necessarily increases h_c. The DSR topology's best optimized eddy current coupling is a remarkable 30% lighter than the best optimized SSR eddy current coupling. Considering the difference in optimized results between the topologies' best machines, it is clear that DSR is the better topology from a mass perspective.

The analytical model leads to slight errors between the calculated and simulated performances of the optimized machine. The error is smaller for the SSR topology than that for the DSR topology but still acceptable for both. The small error between the analytical model and transient 3-D FE simulation results for both topologies justifies the use of the analytical model for low slip values.

C. Comparison of the Analytical and 3-D FE Results of the Best Optimized Topology

To investigate the optimized 60-pole eddy current coupling of the DSR topology, 3-D FE transient simulations are done for a range of slip values. The results are shown in Fig. 19, along with the analytical model's calculated results for the same slip values. There is a good correlation between the 3-D FE and analytically calculated results for slip values up to 15%. For slip values below 15% or fundamental current frequencies lower than 11.25 Hz, the error of the analytical calculation is less than 4.5%, with an error of 2.3% at the rated slip.

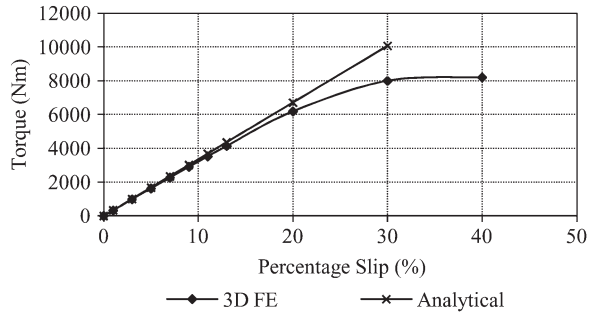

Fig. 19. Analytical and 3-D FE torque versus slip behavior of the optimum designed DSR eddy current coupling.

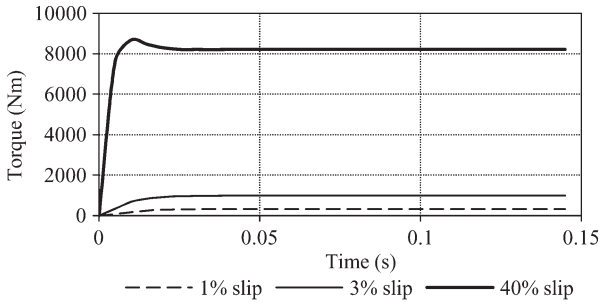

Fig. 20. Three-dimensional FE transient solution of the torque of the optimum designed DSR eddy current coupling at 1%, 3%, and 40% slip speeds.

The breakdown torque of the eddy current coupling is very high at 8215 N · m, reached at a slip of 40%. It is significantly better than the 2.0 per unit minimum specification in Table IV. The 3-D FE transient solutions of the torque of the optimized eddy current coupling are shown in Fig. 20 at 1%, 3% (rated), and 40% slip speeds. As shown, the eddy current coupling generates no torque ripple at these slip speeds.

X. CONCLUSION

In this paper, it has been shown that an eddy current coupling has no cogging and load torque ripples, which are known problems in the SS-PMG.

Using a small prototype eddy current coupling, it has been shown that transient 2-D FE simulations are inaccurate in the performance prediction of the proposed eddy current couplings. Transient 3-D FE simulations, however, show excellent correlation with the measured results of a small prototype as well as a 15-kW manufactured eddy current coupling.

An accurate slip frequency analytical model for large-diameter high torque eddy current couplings has been proposed. The analytical model is very accurate up to 15% slip, which is significantly higher than the rated slip (typically 3%–5%) of eddy current couplings for the SS-PMG.

It has been shown that the optimal designs of the DSR topology are significantly lighter than the optimal designs of the SSR topology due to stray flux constraints. The stray flux constraints cause the optimal design for minimum mass to be a balance between pole number and PM length.

In this paper, the design focus has been on low active mass; however, the economical design and manufacturing of eddy current couplings require further investigation.

REFERENCES

[1] J. H. J. Potgieter and M. J. Kamper, "Design of a new concept direct grid-connected slip-synchronous permanent-magnet wind generator," *IEEE Trans. Ind. Appl.*, vol. 48, no. 3, pp. 913–922, May/Jun. 2012.

[2] J. H. J. Potgieter and M. J. Kamper, "Torque and voltage quality in design optimization of low-cost non-overlap single layer winding permanent magnet wind generators," *IEEE Trans. Ind. Electron.*, vol. 59, no. 5, pp. 2147–2156, May 2012.

[3] S. Huang, M. Aydin, and T. A. Lipo, "Torque quality assessment and sizing optimization for surface mounted permanent magnet machines," in *Proc. 36th Ind. Appl. Conf.*, 2001, pp. 1163–11610.

[4] J. H. J. Potgieter and M. J. Kamper, "Optimum design and technology evaluation of slip permanent magnet generators for wind energy applications," in *Proc. IEEE ECCE*, Raleigh, NC, USA, 2012, pp. 2342–2349.

[5] Z. Mouton and M. J. Kamper, "Design of an eddy-current coupling for slip-synchronous permanent magnet wind generators," in *Proc. 20th ICEM*, Marseille, France, 2012, pp. 633–639.

[6] G. Gail, T. Hartkopf, E. Tröster, M. Höffling, M. Henschel, and H. Schneider, "Static and dynamic measurements of a permanent magnet induction generator: Test results of a new wind generator concept," in *Recent Developments of Electrical Drives*. Darmstadt, Netherlands: Springer-Verlag, 2006, ch. III, pp. 375–384.

[7] M. Pucci and M. Cirrincione, "Neural MPPT control of wind generators with induction machines without speed sensors," *IEEE Trans. Ind. Electron.*, vol. 58, no. 1, pp. 37–47, Jan. 2011.

[8] S. Nishikata and F. Tatsuta, "A new interconnecting method for wind turbine generators in a wind farm and basic performances of the integrated system," *IEEE Trans. Ind. Electron.*, vol. 57, no. 2, pp. 468–475, Feb. 2010.

[9] M. N. Slepchenkov, K. Smedley, and J. Wen, "Hexagram-converter-based STATCOM for voltage support in fixed-speed wind turbine generation systems," *IEEE Trans. Ind. Electron.*, vol. 58, no. 4, pp. 1120–1131, Apr. 2011.

[10] A. Garces and M. Molinas, "A study of efficiency in a reduced matrix converter for offshore wind farms," *IEEE Trans. Ind. Electron.*, vol. 59, no. 1, pp. 184–193, Jan. 2012.

[11] V. Jalili-Marandi, L.-F. Pak, and V. Dinavahi, "Real-time simulation of grid-connected wind farms using physical aggregation," *IEEE Trans. Ind. Electron.*, vol. 57, no. 9, pp. 3010–3021, Sep. 2010.

[12] N. Denniston, A. Massoud, S. Ahmed, and P. Enjeti, "Multiple-module high-gain high-voltage dc–dc transformers for offshore wind energy systems," *IEEE Trans. Ind. Electron.*, vol. 58, no. 5, pp. 1877–1886, May 2011.

[13] U. Hoffmann, P. Bouwer, and M. J. Kamper, "Direct grid connection of a slip-permanent magnet wind turbine generator," in *Proc. IEEE ECCE*, Phoenix, AZ, USA, 2011, pp. 2373–2380.

[14] P. Bouwer, J. H. J. Potgieter, and M. J. Kamper, "Modelling and dynamic performance of a direct-drive direct-grid slip permanent magnet wind generator," in *Proc. IEEE IEMDC*, Niagara Falls, ON, Canada, 2011, pp. 137–142.

[15] E. J. Davies, "An experimental and theoretical study of eddy-current couplings and brakes," *IEEE Trans. Power App. Syst.*, vol. 82, no. 67, pp. 401–419, Aug. 1963.

[16] M. G. Malti and R. Ramakumar, "Three-dimensional theory of the eddy-current coupling," *IEEE Trans. Power App. Syst.*, vol. 82, no. 68, pp. 793–800, Oct. 1963.

[17] S. E. Gay and M. Ehsani, "Analysis and experimental testing of a permanent magnet eddy-current brake," in *Proc. IEEE Conf. Veh. Power Propulsion*, 2005, pp. 756–765.

[18] J. A. Stegmann and M. J. Kamper, "Design aspects of double-sided rotor radial flux air-cored permanent-magnet wind generator," *IEEE Trans. Ind. Appl.*, vol. 47, no. 2, pp. 767–778, Mar./Apr. 2011.

[19] R.-J. Wang, M. J. Kamper, K. Van der Westhuizen, and J. Gieras, "Optimal design of a coreless stator axial flux permanent-magnet generator," *IEEE Trans. Magn.*, vol. 41, no. 1, pp. 55–64, Jan. 2005.

[20] M. J. Kamper, R.-J. Wang, and F. G. Rossouw, "Analysis and performance of axial flux permanent-magnet machine with air-cored nonoverlapping concentrated stator windings," *IEEE Trans. Ind. Appl.*, vol. 44, no. 5, pp. 1495–1505, Sep./Oct. 2008.

[21] G. Venter, "Review of optimization techniques," in *Encyclopedia of Aerospace Engineering*, vol. 8, R. Blockley and W. Shyy, Eds. New York, NY, USA: Wiley, 2010, ch. 428.

Zac Mouton (S'12) received the B.Eng. degree in electrical and electronic engineering, and the M.Sc. (Eng.) degree from the University of Stellenbosch, Stellenbosch, South Africa, in 2010 and 2013, respectively.

His research focus is wind power generation using permanent magnet machine technologies, including the use of eddy current couplings and computer-aided design.

Maarten J. Kamper (SM'08) received the M.Sc. (Eng.) and Ph.D. (Eng.) degrees from the University of Stellenbosch, Stellenbosch, South Africa, in 1987 and 1996, respectively.

Since 1989, he has been with the Academic Staff of the Department of Electrical and Electronic Engineering, University of Stellenbosch, where he is currently a Professor of electrical machines and drives. He is a South African National Research Foundation supported scientist. His research interests include computer-aided design and control of reluctance, permanent magnet, and induction electrical machine drives, with applications in electric transportation and renewable energy.

Prof. Kamper is a Registered Professional Engineer in South Africa.